

# VLT optical observations of the isolated neutron star RX J0420.0–5022<sup>\*</sup>

R. P. Mignani<sup>1</sup>, C. Motch<sup>2</sup>, F. Haberl<sup>3</sup>, S. Zane<sup>1</sup>, R. Turolla<sup>4,1</sup>, and A. Schwöpe<sup>5</sup>

<sup>1</sup> Mullard Space Science Laboratory, University College London, Holmbury St. Mary, Dorking, Surrey, RH5 6NT, UK

<sup>2</sup> CNRS, Université de Strasbourg, Observatoire Astronomique, 11 rue de l'Université, 67000 Strasbourg, France

<sup>3</sup> Max Planck Institut für Extraterrestrische Physik, Giessenbachstrasse, D85748, Garching, Germany

<sup>4</sup> Department of Physics, University of Padua, via Marzolo 8, Padua, 35131, Italy

<sup>5</sup> Astrophysikalisches Institut Potsdam, An der Stenwarte 16, D14482, Potsdam, Germany

Received ...; accepted ...

## ABSTRACT

**Context.** X-ray observations performed with the *Röntgen Satellite* (*ROSAT*) led to the discovery of seven radio-silent isolated neutron stars (INSs) which are detected only through the relatively dim and purely thermal X-ray emission from the cooling star surface. A few of these INSs (a.k.a. X-ray Dim INSs, or XDINSs) have been also detected at optical wavelengths where they seem to feature thermal spectra. Optical studies of XDINSs thus play a crucial role in mapping the temperature distribution on the neutron star surface and in investigating the existence of an atmosphere around the neutron star.

**Aims.** The aim of this work is to investigate the optical identification of the XDINS RX J0420.0–5022, tentatively proposed by Haberl et al. (2004) based on *Very Large Telescope* (*VLT*) observations.

**Methods.** We re-analysed the original observations of Haberl et al. (2004) to assess the detection significance of the proposed counterpart and we performed deeper *VLT* observations aiming at a higher confidence detection.

**Results.** With a  $\sim 2\sigma$  detection significance and a re-computed flux of  $B = 27.52 \pm 0.61$ , we can not rule out that the proposed counterpart was spurious and produced by the halo of a very bright nearby star. While we could not detect the proposed counterpart in our deeper *VLT* observations, we found evidence for a marginally significant ( $\sim 3.9\sigma$ ) detection of a similarly faint object ( $B = 27.5 \pm 0.3$ ),  $\approx 0''.5$  north of it and coincident with the updated *Chandra* position of RX J0420.0–5022. Interestingly, the angular separation is consistent with the upper limit on the RX J0420.0–5022 proper motion (Motch et al. 2009), which suggests that we might have actually detected the Haberl et al. proposed counterpart. From the flux of the putative RX J0420.0–5022 counterpart we can rule out a  $> 7$  optical excess with respect to the extrapolation of the *XMM-Newton* spectrum.

**Conclusions.** High spatial resolution observations with the refurbished *Hubble Space Telescope* (*HST*) are the only way to confirm the detection of the putative candidate counterpart and to validate its identification with RX J0420.0–5022.

**Key words.** Optical: stars; neutron stars: individual RX J0420.0–5022

## 1. Introduction

X-ray observations performed with the *Röntgen Satellite* (*ROSAT*) yielded to the identification of a group of seven radio-silent (Kondratiev et al. 2008)<sup>1</sup> Isolated Neutron Stars (INSs). Their relatively dim X-ray emission ( $L_X \approx 10^{30}$ – $10^{31}$  erg s<sup>−1</sup>) originally earned them the nickname of X-ray Dim INSs, or XDINSs (see Haberl 2007; van Kerkwijk & Kaplan 2007, and Kaplan 2008 for recent reviews). Recently, a new XDINS candidate has been identified in archival *XMM-Newton* observations (Pires et al. 2009). XDINSs have purely thermal X-ray spectra which are best represented by a blackbody ( $kT \approx 50$ – $100$  eV), as expected for middle-aged ( $\sim 1$  Myr) cooling INSs, whose emission radius is consistent with a sizable fraction of the neutron star surface. The derived hydrogen column densi-

ties  $N_H \approx 10^{20}$  cm<sup>−2</sup> suggest distances  $< 500$  pc (Posselt et al. 2007), as confirmed in two cases by their optical parallaxes (e.g. van Kerkwijk & Kaplan 2007). X-ray pulsations ( $P = 3$ – $12$  s) have been detected for all of them (Haberl et al. 1997, 1999; Haberl & Zavlin 2002; Hambaryan et al. 2002; Zane et al. 2005; Tiengo & Mereghetti 2007) but RX J1605.3+3249, although with different pulsed fractions. The measurement of the period derivative  $\dot{P}$  (Cropper et al. 2004; Kaplan & van Kerkwijk 2005a; Kaplan & van Kerkwijk 2005b; van Kerkwijk & Kaplan 2008) yielded spin-down ages of  $\sim 1.5$ – $3.8$  Myrs and rotational energy losses  $\dot{E} \sim (3$ – $5) \times 10^{30}$  erg s<sup>−1</sup>. Broad absorption features ( $E_{\text{line}} \approx 0.2$ – $0.7$  keV) have been observed in all XDINSs but RX J1856.5–3754 (Haberl et al. 2003, 2004; van Kerkwijk et al. 2004; Zane et al. 2005), superimposed to the thermal continuum. These features are likely due to proton cyclotron and/or bound-free, bound-bound transitions in H, H-like and He-like atoms. The inferred magnetic fields of  $\sim 10^{13}$ – $10^{14}$  G are consistent with the values derived from the neutron star spin down and suggest that XDINSs might be (evolutionary) linked to other class of INSs, the magne-

Send offprint requests to: R. P. Mignani; rm2@mssl.ucl.ac.uk

<sup>\*</sup> Based on observations collected at ESO, Paranal, under Programmes 66.D-0128(A), 078.D-0162(A)

<sup>1</sup> The claimed low-frequency pulsed emission from two of them (Malofeev et al. 2007) has not been confirmed yet.

tar candidates (see Mereghetti 2008 for a recent review) and the Rotating Radio Transients (e.g. Popov, Turolla, Possenti 2006).

In the optical, only RX J1856.5–3754 (Walter & Matthews 1997; Walter 2001), RX J0720.4–3125 (Motch & Haberl 1998; Kulkarni & van Kerkwijk; 1998; Motch et al. 2003) and RX J1605.3+3249 (Kaplan et al. 2003; Motch et al. 2005; Zane et al. 2006) have counterparts certified by their proper motion measurements, while likely candidates have been proposed for RX J1308.6+2127 (Kaplan et al. 2002) and 1RXS J214303.7+065419 (Zane et al. 2008; Schwöpe et al. 2009) based on their coincidence with the X-ray positions. Apart from providing a clear evidence of the optical identification, proper motion measurements are important to obtain an estimate of the kinematic age of the neutron star, to be compared with the characteristic age derived from the spin-down. The XDINS optical fluxes usually exceed by a factor of  $\sim 5$  (or more) the extrapolation of the X-ray blackbody, and their optical spectra, when measured, seem to follow a Rayleigh-Jeans distribution (e.g., Kaplan 2008). The XDINS optical emission has been interpreted either in terms of a non-homogeneous surface temperature distribution, with the cooler part emitting the optical (e.g., Pons et al. 2002), or of reprocessing of the surface radiation by a thin H atmosphere around a bare neutron star (Zane et al. 2004; Ho 2007), or of non-thermal emission from particles in the star magnetosphere (Motch et al. 2003). However, for the measured  $\dot{E}$ , magnetospheric emission would not be detectable, at least if an average optical emission efficiency of rotation-powered neutron stars (e.g. Zharikov et al. 2006) is assumed. Alternatively, like for the magnetars, optical magnetospheric emission might be powered by the neutron star magnetic field, as proposed for 1RXS J214303.7+065419 (Zane et al. 2008).

One of the XDINSs without a certified optical counterpart is RX J0420.0–5022. The first optical observations of the field performed with the *New Technology Telescope* (NTT) soon after the discovery of the X-ray source (Haberl et al. 1999) did not reveal any candidate counterpart brighter than  $B \sim 25.2$  and  $R \sim 25.2$ . More recently, thanks to the updated *Chandra* position, a possible optical identification was proposed by Haberl et al. (2004) with a faint object ( $B = 26.6 \pm 0.3$ ,  $V \geq 25.5$ ) tentatively detected on archival *Very Large Telescope* (VLT) images. However, the identification has not been confirmed so far. The field of RX J0420.0–5022 was also observed in the near-infrared (NIR) with the VLT but no candidate counterpart was detected down to  $H \sim 21.7$  (Mignani et al. 2007; Lo Curto et al. 2007; Posselt et al. 2009) and  $K_s \sim 21.5$  (Mignani et al. 2008). In this paper we re-analyze the original VLT observations of RX J0420.0–5022 presented by Haberl et al. (2004) and we report on follow-up, longer optical observations of the candidate counterpart, performed by our team with the VLT. Observations and data analysis are described in Sect. 2, while results are presented and discussed in Sect. 3 and Sect. 4, respectively.

## 2. Observations

### 2.1. Observation description

Optical observations of RX J0420.0–5022 were performed in service mode with the VLT at the ESO Paranal observatory on November 21st 2000, on November 25th 2006,

**Table 1.** Log of the VLT *FORs1* and *FORs2* B-band observations of RX J0420.0–5022). Columns report the observing date (yyyy-mm-dd), the number of exposures (N) and the total integration time per night (T), the image quality (IQ) and rms (in parentheses), as computed on the image, and the airmass. Values are the average computed over the exposure sequence.

	Date	N	T (s)	IQ (")	Airmass
FORs1	2000-11-21	3	3600	0.74 (0.08)	1.14
FORs2	2006-11-25	5	2915	0.71 (0.10)	1.24
	2007-01-16	10	5830	0.93 (0.18)	1.18
	2007-01-22	5	2915	0.82 (0.11)	1.19
	2007-02-11	5	2915	0.82 (0.12)	1.30

January 16th and 22nd, and February 11th 2007 (see Tab. 1 for a summary). The 2000 observations were performed with *FOcal Reducer/low dispersion Spectrograph* (*FORs1*), a multi-mode camera for imaging and long-slit/multi-object spectroscopy, as part of the ESO guaranteed time programme. At the epoch of the observations *FORs1* was equipped with the original four port 2048×2084 CCD detector and it was mounted at the VLT Antu telescope. The observations were performed in standard resolution mode, with a 0".2 pixel size and a field of view of  $6'.8 \times 6'.8$ . The low gain, fast read-out, single port mode was chosen. A sequence of three 1200 s exposures was obtained through the Bessel B filter, with an airmass of  $\sim 1.14$ , an image quality of  $\sim 0''.7$ , and dark time conditions. Since the seeing values measured by the differential image motion monitor (DIMM) are relative to the zenith and not to the pointing direction of the telescope they are not necessarily indicative of the actual image quality. We thus computed the actual image quality from the measured point spread function (PSF), derived by fitting the full width half maximum (FWHM) of a number of well-suited field stars using the *SExtractor* tool (Bertin & Arnouts 1996), as documented in the *FORs1* data quality control pages<sup>2</sup>.

Two 600 s additional exposures were obtained in the V filter but since the proposed candidate counterpart was not detected we focus our analysis on the B-band data only. Sky conditions were reported to be photometric (see Haberl et al. 2004 for a more detailed observations description). A very bright star, CD-50 1353 ( $B = 9.9$ , as listed in *Simbad*), located at  $\approx 45''$  from the position of RX J0420.0–5022 was partially masked using the *FORs1* occulting bars. Bias, twilight flat-fields frames, and images of the standard star fields SA 92 and Rubin 149 (Landolt 1992) were obtained as part of the *FORs1* science calibration plan.

The 2006/2007 observations were performed with *FORs2* as part of the ESO open time programme. At the epoch of the observations, *FORs2* had swapped with *FORs1* at the VLT Antu telescope. *FORs2* is equipped with two 2k×4k MIT CCD detectors. Due to vignetting, the effective sky coverage of the two detectors is smaller than the projected detector field of view, and it is larger for the upper CCD chip. Observations were performed in high resolution mode, with a 2×2 binning and a pixel size of 0".125. The low gain, fast read-out mode was chosen. The telescope pointing was set in order to position RX J0420.0–5022 in

<sup>2</sup> <http://www.eso.org/observing/dfo/quality/FORs1/qc/qc1.html>

the upper CCD chip to include a larger number of reference stars for a precise image astrometry thanks to its larger effective sky coverage ( $3'5 \times 2'$ ). Sequences of 580 s exposures were obtained through the Bessel B filter. The bright star CD-50 1353 was more efficiently masked both by positioning it at the centre of the gap between the two chips and by using the *FORS2* occulting bars. Unfortunately, the distance of RX J0420.0–5022 from the gap ( $\sim 17''$ ) and the width of the occulting bars ( $\sim 25''$ ), which can move along one CCD direction only, made it impossible to mask completely the star halo. Exposures were taken in dark time and under mostly clear but not perfectly photometric sky conditions. In particular, the night of February 11th was affected by the presence of thin variable cirri. Atmospheric conditions were not optimal either. The first two nights were affected by a strong wind, close to the telescope pointing limit, while the nights of January 16th and February 11th were affected by 40 % humidity. Unfortunately, although foreseen by the instrument science calibration plan, only for some nights both day and night time calibration frames were taken. In particular, no twilight flat-fields were taken for the night of November 25th, while B-band standard star images (of the Rubin 152 field) were taken on the night of February 11th only.

## 2.2. Data reduction and calibration

We retrieved the *FORS1* science images from the public ESO archive<sup>3</sup> and we reduced them using tools available in *MIDAS* for bias subtraction, and flat-field correction. The same reduction steps were applied to the *FORS2* science images through the ESO *FORS2* data reduction pipeline<sup>4</sup>. We searched the archive for suitable twilight flat-fields to reduce the *FORS2* November 25th science images but the closest in time were those associated with our January 16th images. We evaluated the possibility of using lamp flat-fields as backup calibration frames, with the caveat that they are affected by reflections produced by the instrument atmospheric dispersion correctors. However, since lamp flat-fields are only taken for trending purposes, and the high resolution mode is not the standard one for *FORS2*, no suitable data was found in the archive. Thus, since the November 25th science images can not be calibrated with twilight flat-fields taken on the same night, initially we do not use them in the subsequent analysis. For both the *FORS1* and *FORS2* data sets the photometric calibration was applied using the available, extinction corrected, night zero points available through the instrument data quality control database<sup>5</sup>. For the January 16th and 22nd *FORS2* observations, for which no standard star images were taken, we assumed as a zero point the value extrapolated from the night zero point trend. Since none of the *FORS2* observations was taken in perfectly photometric conditions, we estimated that a relative photometry calibration, with the February 11th observations taken as a reference, would introduce an uncertainty comparable to that associated to the extrapolation of the zero point trend. We converted the trended *FORS1* and *FORS2* zero points, computed in units of electrons/s, to units of ADU/s by applying the corresponding electrons-to-ADU conver-

sion factors. For each of the two data sets, we then used the *MIDAS* task *average/window* to cosmic rays filter and stack single exposures.

## 2.3. Astrometry

As a reference for the astrometric calibration we used the *GSC-2* version 2.3 (Lasker et al. 2008). Approximately 70 *GSC-2* objects are identified in the 2000 *FORS1* image. From this list we filtered out extended objects, stars that are either saturated or too faint to be used as reliable astrometric calibrators or too close to the CCD edges. We finally performed our astrometric calibration using 30 well-suited *GSC-2* reference stars, evenly distributed in the *FORS1* field of view. The pixel coordinates of the selected *GSC-2* stars were measured by fitting their intensity profiles with a Gaussian function using the dedicated tool of the *Graphical Astronomy and Image Analysis* (*GAIA*) interface<sup>6</sup>. The coordinate transformation between the detector and the celestial reference frame was then computed using the *Starlink* package *ASTROM*<sup>7</sup> using higher order polynomials to account for the CCD distortions. The rms of the astrometric solution turned out to be  $\approx 0''.2$ , accounting for the rms of the fit in the right ascension and declination components. Following Lattanzi et al. (1997), we estimated the overall uncertainty of our astrometry by adding in quadrature the rms of the astrometric fit and the precision with which we can register our field on the *GSC-2* reference frame. This is estimated as  $\sqrt{3} \times \sigma_{GSC} / \sqrt{N_s}$ , where the  $\sqrt{3}$  term accounts for the free parameters (x-scale, y-scale, and rotation angle) in the astrometric fit,  $\sigma_{GSC}$  is the mean positional error of the *GSC-2* coordinates ( $0''.3$ , Lasker et al. 2008) and  $N_s$  is the number of stars used for the astrometric calibration. The uncertainty on the reference stars centroids is below  $0''.01$  and was neglected. We also added in quadrature the  $0''.15$  uncertainty (Lasker et al. 2008) on the tie of the *GSC-2* to the International Celestial Reference Frame (ICRF). Thus, the overall accuracy of the *FORS1* astrometry is  $0''.27$  ( $1\sigma$ ). The astrometric calibration of the *FORS2* image was computed in the same way but with a lower number of reference stars due to the smaller field of view of the *FORS2* chip. The rms of the astrometric fit then turned out to be  $0''.36$ . Again, after accounting for systematic uncertainties (see above) the overall accuracy of the *FORS2* astrometry is  $0''.43$  ( $1\sigma$ ).

As a reference to compute the RX J0420.0–5022 position we considered X-ray coordinates derived from *Chandra* observations which are closest in time to our *VLT* observations. In particular, for the *FORS1* observations (epoch 2000.89) we used the *Chandra* coordinates (epoch 2002.86) published in Haberl et al. (2004), i.e.  $\alpha_{J2000} = 04^h20^m01.95^s$ ,  $\delta_{J2000} = -50^\circ22'48''.1$  which have a nominal error of  $0''.6$  (90% confidence level). For the *FORS2* observations (epoch 2007.04) we reanalysed a more recent *Chandra* observations (epoch 2005.85). Like in Haberl et al. (2004), we determined the source position with the *CIAO* task *celldetect* and we obtained  $\alpha_{J2000} = 04^h20^m01.94^s$ ,  $\delta_{J2000} = -50^\circ22'48''.2$  ( $0''.6$ ; 90% confidence level). As shown in Haberl et al. (2004) a match between the coordinates of the X-ray sources detected in the *Chandra* field with those of their possible *USNOB.10* counterpart did

<sup>3</sup> <http://archive.eso.org>

<sup>4</sup> <http://www.eso.org/observing/dfo/quality/FORS2/pipeline>

<sup>5</sup> <http://www.eso.org/observing/dfo/quality/FORS2/qc/qc1.html>

<sup>6</sup> [star-www.dur.ac.uk/~pdraper/gaia/gaia.html](http://star-www.dur.ac.uk/~pdraper/gaia/gaia.html)

<sup>7</sup> <http://star-www.rl.ac.uk/Software/software.htm>

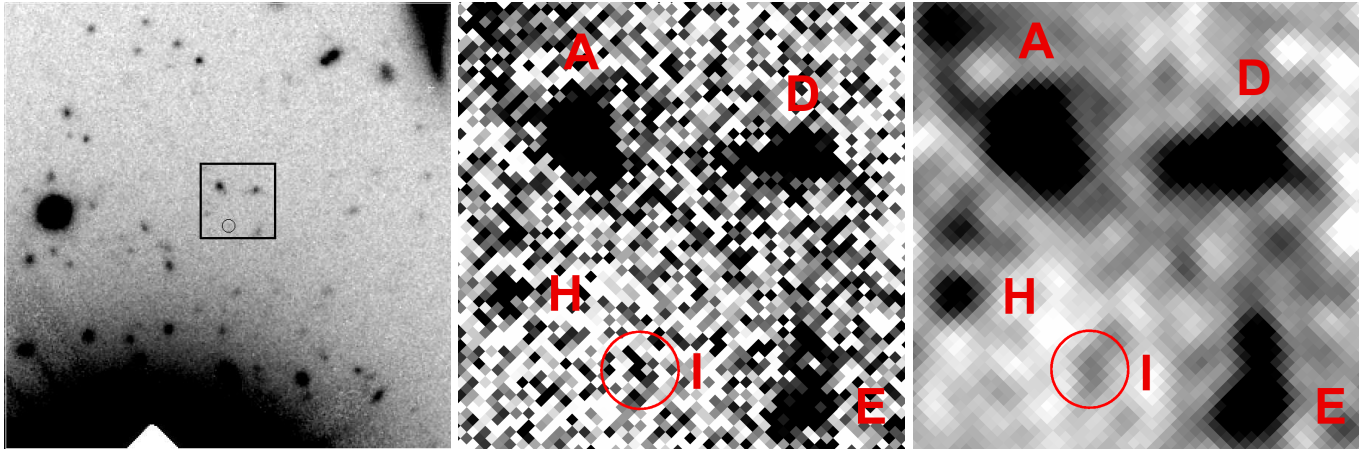


**Fig. 1.** Left panel:  $1' \times 1'$  cutout of the coadded *FORs1* B-band image (3600 s) of the RX J0420.0–5022 field. North to the top, east to the left. The RX J0420.0–5022 position lies at the centre of the  $10'' \times 10''$  square and is indicated by the circle. The radius of the circle ( $0''.87$ ; 90% confidence level) represents the uncertainty on the computed 2000 RX J0420.0–5022 position (see Sect. 2.3), which accounts for the absolute accuracy of the *Chandra* coordinates at the reference epoch, the uncertainty on the proper motion extrapolation at the observing epoch, and the accuracy of our astrometric calibration. The white triangle at the bottom of the image is the edge of the *FORs1* occulting bar. Middle panel: Enlargement of the  $10'' \times 10''$  region after sky background subtraction. The intensity scale has been adjusted for a better visualisation of the faintest objects in the field. Objects labelling is as in Haberl et al. (2004). The faint feature labelled *I* is their proposed candidate counterpart. Right panel: image of the same region smoothed with a Gaussian filter over cells of  $3 \times 3$  pixels.

not reveal any significant systematic shift. No significant shift is found between the coordinates of the same X-ray sources between the 2002 and 2007 *Chandra* observations either. Thus, no boresight correction was applied to our reference coordinates. Recently, an upper limit on the RX J0420.0–5022 proper motion ( $123 \text{ mas yr}^{-1}$ ,  $2\sigma$ ) was obtained with *Chandra* (Motch et al. 2009). We accounted for the proper motion uncertainty when we registered the reference *Chandra* coordinates on the *FORs1* and on the *FORs2* images. This yields an additional position uncertainty due to the unknown proper motion of  $\sim 0''.123$  and  $\sim 0''.073$  ( $1\sigma$ ) for each of the two images, respectively. The overall uncertainty to be attached to the RX J0420.0–5022 position at the epoch of the *FORs1* and *FORs2* observations was finally obtained by adding in quadrature the error on the *Chandra* coordinates ( $1\sigma$ ), the coordinate uncertainty due to the proper motion, and the overall error of the astrometric calibration. This yields to uncertainties of  $0''.87$  and  $1''.11$  (90% confidence level) on the RX J0420.0–5022 position on the *FORs1* and on the *FORs2* image, respectively.

### 3. Results

#### 3.1. The *FORs1* observations

We first re-analyzed the *VLT* observations taken in 2000 to better assess the confidence of the optical identification of RX J0420.0–5022 proposed in Haberl et al. (2004). Fig. 1 (left) shows the computed *Chandra* position of RX J0420.0–5022 overlaid on a cutout of the 2000 *FORs1* co-added B-band image. As seen from Fig. 1 (left), only the bright PSF core of star CD-50 1353 is masked, while its halo extends close to the target position. This increases the local sky background as well as the background noise, which results in a larger number of spurious detections. In order to enhance the detection significance for fainter ob-

jects we tried to minimise the effects of the halo of star CD-50 1353 on the local sky background. Firstly, we fitted the sky background in an area of  $\sim 15'' \times 15''$  around the target position using a second order polynomial and we subtracted the fitted value from the co-added B-band image using the *MIDAS* task `fit/flat.sky`. We warn here that the fit to the sky background is biased by the choice of the sampling areas. This can yield to more or less evident feature enhancements when the sky background subtraction is applied to the image. We thus carefully choose the sampling areas not to introduce systematic effects in our procedure. Fig. 1 (middle) shows a zoom of the sky-subtracted image. As already shown by Haberl et al. (2004), four objects are clearly detected close to the *Chandra* position. In addition, a very faint feature is possibly recognised within the *Chandra* error circle. We identify this feature with object *I* of Haberl et al. (2004), which they tentatively proposed as a candidate counterpart to RX J0420.0–5022. However, the excess of counts at the feature position is comparable to the rms of the local sky background, which corresponds to a very low detection significance of  $\approx 2\sigma$ . We re-computed the magnitude of the feature through PSF photometry. We derived the PSF parameters from a set of several non saturated objects selected for their stellar like profiles, located close to the RX J0420.0–5022, and spanning a large range of magnitudes. The airmass correction was applied using the Paranal extinction coefficients measured with *FORs1*<sup>8</sup>. We found  $B = 27.52 \pm 0.61$ . This is fainter than the value of  $B = 26.57 \pm 0.30$  reported in Haberl et al. (2004) but it is still compatible at the  $1\sigma$  level when systematic uncertainties in their photometry are taken into account (see section 3 of Haberl et al.). For a better visualisation, we smoothed the image using a Gaussian filter over cells of  $3 \times 3$  pixels i.e. of size comparable to that of the image PSF. Since the image smoothing enhances the detection of very

<sup>8</sup> <http://www.eso.org/observing/dfo/quality/FORS1/qc/qc1.html>



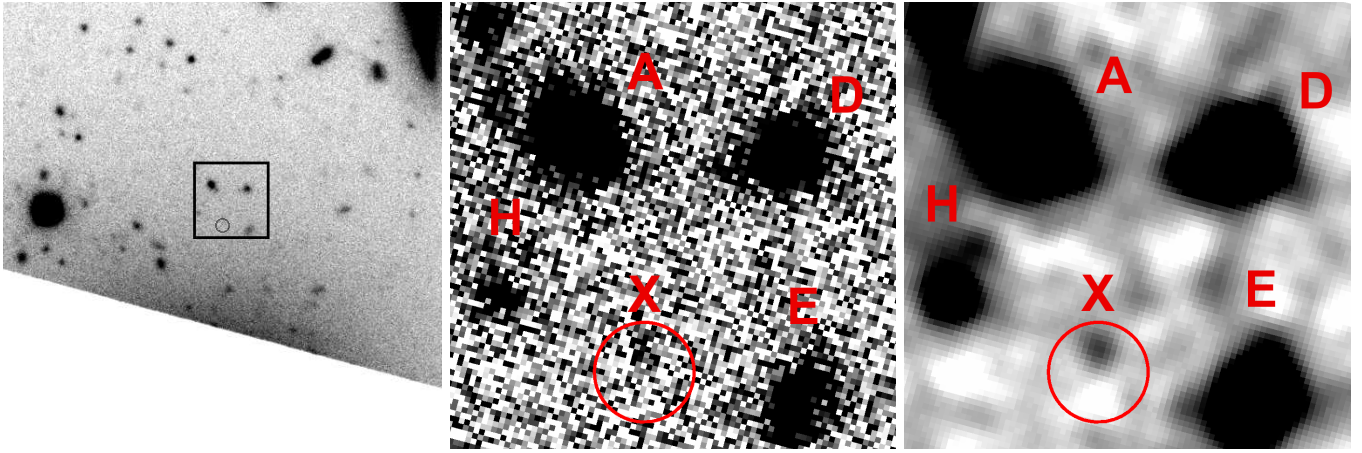


**Fig. 2.** Left panel:  $1' \times 1'$  cutout of the co-added *FORS2* B-band image (7540 s) obtained by the co-addition of the January/February 2007 best image quality exposures. North to the top, east to the left. The circle ( $1''.11$  radius; 90 % confidence level) corresponds to the uncertainty on the computed RX J0420.0–5022 position (see Sect. 2.3). The white band in the left panel corresponds to the gap between the two CCD chips. Middle panel: zoomed image of the inner  $10'' \times 10''$  region (marked by a square) after co-addition of all the available exposures (see text), rebinning, and sky background subtraction. Right panel: image of the same region smoothed with a Gaussian filter over cells of  $5 \times 5$  pixels. The faint feature detected within the *Chandra* error circle is labelled X.

faint objects but also that of fluctuations of the noisy sky background we fine-tuned the smoothing parameters not to produce an over-enhancement of background features. The result is shown in Fig. 1 (right). However, the image processing (sky subtraction and smoothing) does not single out object *I* against the many, similarly significant, background features recognised around the *Chandra* position. Thus, we can not rule out that object *I* was a spurious detection due to the high background noise induced by the halo of star CD-50 1353.

### 3.2. The *FORS2* observations

We used our follow-up *FORS2* observations to search for a higher confidence candidate counterpart to RX J0420.0–5022. In order to minimise the effects of the halo of star CD-50 1353, we first co-added only the exposures taken with an image quality better than  $1''$ . In first place, we used the co-addition of the best image quality exposures of all nights with the exception of those taken on November 25th 2006, which were calibrated using twilight flat-fields taken about 40 days apart (see Sect 2.2).

Fig. 2 (left) shows the computed *Chandra* position of RX J0420.0–5022 overlaid on a cutout of the *FORS2* B-band image (6960 s) obtained from the co-addition of the twelve best image quality ( $0''.8$ – $0''.9$ ) January/February 2007 exposures. Indeed, although the more efficient masking reduced the contamination from the halo of star CD-50 1353, the sky background at the *Chandra* position remained significantly affected by scattered light. As we did in Sect. 3.1, we fitted and subtracted the sky background from the co-added image. In order to increase the S/N ratio per pixel we then rebinned the sky-subtracted image by a factor of 2, ending up with a pixel size of  $0''.25$  which well matches that of *FORS1* ( $0''.2$ ). We did not find evidence for object *I*, the feature tentatively proposed by Haberl et al. (2004) as a candidate counterpart to RX J0420.0–5022. However, we possibly recognised a second feature within the *Chandra* error circle,  $\approx 0''.5$  north of the expected

position of object *I*. Unfortunately, the low number of counts only yields to a marginal detection significance ( $\sim 3\sigma$ ). As a test, and being aware of possible issues related to the non optimal flat-fielding, we decided to use the five November 2006 exposures (2915 s) which happen to have the best image quality ( $0''.7$ ) in the *FORS2* data set. As done for the January/February data set, we fitted and subtracted the sky background from the co-added image and we rebinned the sky-subtracted image by a factor of 2. Interestingly, a feature appears right at the same position of that seen in the co-addition of the January/February best image quality exposures, although with only a  $\sim 2.5\sigma$  detection significance. While we do not claim that this is a strong detection evidence, it is quite unusual that a background feature appears at the same position in images taken weeks apart. To increase the S/N ratio, we both co-added all the twenty 2007 exposures (11680 s) and all the available exposures (14575 s), again applying sky-subtraction and rebinning, and we obtained a detection significance of  $\sim 3.5\sigma$  and  $\approx 3.9\sigma$ , respectively. A zoom of the longest integration time, co-added image is shown in Fig. 2 (middle), where the feature detected in the *Chandra* error circle is labelled X. For a better visualisation, we smoothed the image using a Gaussian filter over cells of  $5 \times 5$  pixels (Fig. 2, right).

As done in Sect. 3.1, we measured the flux of object X through PSF photometry. The airmass correction was applied using the Paranal extinction coefficients measured with *FORS2*<sup>9</sup>. Due to the still low S/N in the aperture and to the noisy sky background the flux measurement is obviously affected by a large error. Our best estimate gives  $B = 27.5 \pm 0.3$ , where the statistical error obviously dominates over the uncertainty of our absolute photometry (Sect. 2.2). The object magnitude and coordinates are listed in Table 2 together with those of the other objects identified in Fig. 2, as a reference. Interestingly, the flux of object X coincides with that of object *I* ( $B = 27.52 \pm 0.61$ ), the

<sup>9</sup> <http://www.eso.org/observing/dfo/quality/FORS2/qc/qc1.html>

**Table 2.** Label, coordinates, and  $B$ -band magnitudes of the objects identified in the *FORs2* image (Fig.2; middle). Coordinate uncertainties are derived from our astrometric calibration (Sect. 2.3). A photometry calibration error of 0.05 magnitudes is assumed (Sect. 2.2).

ID	$\alpha_{J2000}^{(hms)}$	$\delta_{J2000}^{(o'")}$	$B$
X	04 20 01.94	-50 22 47.75	$27.5 \pm 0.3$
A	04 20 02.10	-50 22 42.60	$24.35 \pm 0.05$
D	04 20 01.59	-50 22 43.17	$24.95 \pm 0.05$
E	04 20 01.57	-50 22 48.75	$25.37 \pm 0.07$
H	04 20 02.28	-50 22 46.30	$26.49 \pm 0.10$

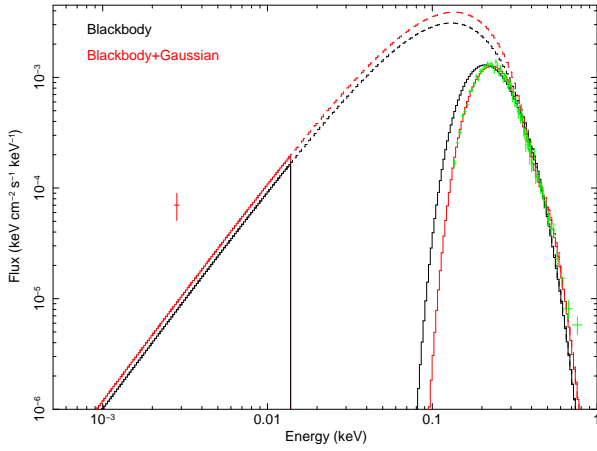


**Fig. 3.** Best fit models to the *XMM-Newton EPIC-pn* spectrum of RX J0420.0–5022 (green data points). The red and black lines correspond to a single blackbody and to a blackbody plus an absorption line spectral fit, respectively (see Sect. 4 for details). Absorption-corrected model curves are drawn as dashed lines. The dereddened B-band flux of the putative candidate counterpart ( $1\sigma$  error) is marked.

candidate counterpart tentatively proposed by Haberl et al. (2004), which we re-computed in Sect. 3.1. One may thus speculate whether we detected the same feature both in the *FORs2* and in the *FORs1* images, although at slightly different positions. The measured angular separation between object X and object I is  $0''.5 \pm 0''.3$ , accounting for an estimated uncertainty of one pixel on the object centroid in both the *FORs1* and *FORs2* images. This would imply a yearly displacement of  $80 \pm 50$  mas yr $^{-1}$ , consistent with the upper limit on the RX J0420.0–5022 proper motion (Motch et al. 2009). The yearly displacement would thus imply a transverse velocity of  $\approx 140 d_{350}$  km s $^{-1}$ , where  $d_{350}$  is the neutron star distance in units of 350 pc (Posselt et al. 2007), i.e. within the range of the tangential velocities inferred for neutron stars. The actual proper motion measurement, to be eventually obtained with *Chandra*, will unambiguously address this speculation.

#### 4. Discussion

The very marginal detection significance ( $\sim 3.9\sigma$ ) of object X against the number of local spurious detections makes it difficult to determine whether or not it is real and, thus, whether or not we have detected a candidate optical

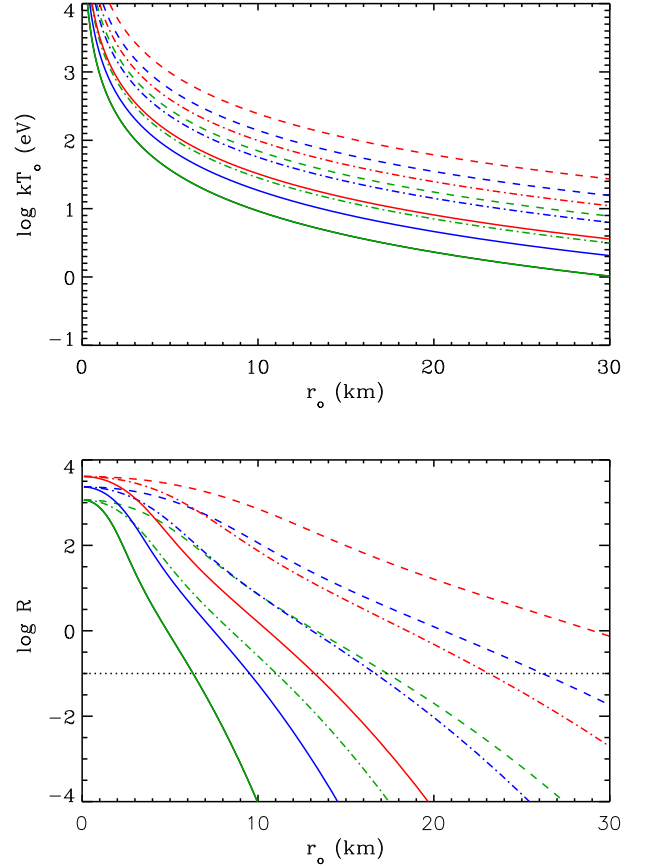


**Fig. 4.** Upper panel: blackbody temperature  $T_o$  as a function of the emission radius  $r_o$  for different values of the optical excess  $f$ . The red, blue, and green lines correspond to an optical excess of  $f = 7, 4$  and  $2$ , respectively. For each value of  $f$ , the three curves are drawn for different values of the neutron star distance, 550, 350 and 200 pc (dashed, dot-dashed, and solid lines, respectively). Lower panel: relative contribution  $R$  to the total 0.1-1keV X-ray flux of a blackbody with temperature  $T_o$  versus the radius of the emitting region  $r_o$  for different values of the optical excess  $f$  and of the source distance. The line style and colour coding is the same as in the upper panel. The horizontal dotted line corresponds to the threshold  $R = 0.1$ . The allowed region in the parameters space lies below this line.

counterpart to RX J0420.0–5022. We compared the flux of the putative candidate counterpart with the extrapolation in the optical domain of the models which best fit the *XMM-Newton EPIC-pn* spectrum of RX J0420.0–5022. To this aim, we have re-analysed the original data of Haberl et al. (2004) using updated calibration files. The spectrum can be fit by a single blackbody with temperature  $kT_X = 46.2 \pm 1.4$  eV and  $N_H = (0.73 \pm 0.21) \times 10^{20}$  cm $^{-2}$  (reduced  $\chi^2 = 2.08$ , 64 d.o.f.), corresponding to an emission radius  $r_X = 5.11 d_{350}$  km, where  $r_X$  is the X-ray emission as seen from infinity and  $d_{350}$  is the neutron star distance in units of 350 pc (Posselt et al. 2007). However, a blackbody with  $kT_X = 47.8 \pm 2.2$  eV and  $N_H = 1.19_{-0.31}^{+0.45} \times 10^{20}$  cm $^{-2}$  ( $r_X = 5.44 d_{350}$  km) plus an absorption line with centroid energy  $E_{line} = 337 \pm 24$  eV and equivalent width  $EW_{line} = 47 \pm 5$  eV gives a better fit (reduced  $\chi^2 = 1.33$ , 62

d.o.f.). The line width  $\sigma_{line}$  was fixed at 70 eV, as in Haberl et al. (2004). For the spectral fits we used element abundances both from Anders & Grevesse (1989) and Wilms et al. (2000), obtaining virtually the same results. The best-fit, absorption-corrected X-ray spectra of RX J0420.0–5022 are shown in Fig. 3 together with the optical flux of its putative counterpart. We corrected for the absorption in the B band using as a reference the  $N_H$  derived from the best-fit X-ray spectral model (blackbody plus absorption line) and applying the relation of Predehl & Schmitt (1995) with the extinction coefficients of Fitzpatrick (1999). From the flux of the putative counterpart we can rule out a  $> 7$  optical excess with respect to the extrapolation of the *XMM-Newton* spectrum. We note that an optical excess of  $\sim 5$  is usually observed in other optically identified XDINSs with the exception of RX J1605.3+3249 and 1RXS J214303.7+065419, where it is as large as  $\approx 15$  (Motch et al. 2005) and  $\approx 30$ –40 (Zane et al. 2008; Schwope et al. 2009), respectively.

As a limit case, we checked whether an optical excess of  $\sim 7$  would be compatible with either rotation-powered emission from the neutron star magnetosphere or with thermal emission from a fraction of the neutron star surface, colder and larger than that responsible for the X-ray emission. In the first case, the value of the X-ray period and the upper limit on the period derivative of RX J0420.0–5022 ( $P = 3.45$  s;  $\dot{P} < 92 \times 10^{-13} \text{ s s}^{-1}$ ; see Haberl 2007) only yield a rotational energy loss  $\dot{E} < 8.8 \times 10^{33} \text{ erg s}^{-1}$ . The flux of the putative counterpart would imply an optical luminosity  $L_B \sim 1.2 \times 10^{27} \text{ erg s}^{-1} d_{350}^2$ . This would correspond to an emission efficiency  $\eta_B \equiv L_B/\dot{E} > 1.3 \times 10^{-7}$ , which could still be compatible with the values expected for  $10^6$ – $10^7$  years old neutron stars (Zharikov et al. 2006). However, a period derivative  $\dot{P} \sim 10^{-13} \text{ s s}^{-1}$ , comparable to that of other XDINSs, would imply a factor of 100 lower  $\dot{E}$  and would make it less likely that the optical emission is powered by the rotational energy loss. In the second case, we can constrain both the blackbody temperature  $T_o$  and the emission radius  $r_o$ , as seen from infinity. Since the fit to the *XMM-Newton* spectrum does not require the presence of a second blackbody component at lower temperature, we can impose that its relative contribution  $R$  to the total X-ray flux in the 0.1–1 keV band (see Sect. 3 of Zane et al. 2008) must be  $\ll 1$ . We chose  $R = 0.1$  as a reasonable threshold. We first computed the values of  $T_o$  for a grid of values of  $r_o$  and for different values of the optical excess  $f = \frac{r_o^2 T_o}{r_X^2 T_X}$  and of the source distance (Fig. 4, upper panel), where  $T_X = 47.8 \text{ eV}$  and  $r_X = 5.44 d_{350} \text{ km}$  are derived from the best X-ray spectral fit (blackbody plus absorption line, see above). We then computed  $R$  from the values of  $r_o$  and  $T_o$  (Fig. 4, lower panel). As it is seen, for a neutron star distance of 350 pc an optical excess of  $\sim 7$  would be compatible with a blackbody with  $kT_o \leq 25 \text{ eV}$  and an implausibly large emitting radius of  $r_o \geq 23 \text{ km}$ . Thus, would our putative counterpart be confirmed, an optical excess of  $\sim 7$ , for a neutron star distance of  $\sim 350 \text{ pc}$ , might rather point towards a non-thermal origin for the optical emission, as proposed for RBS1774 (Zane et al. 2008). Actually, as Fig. 4 shows, unphysical large radii are required even if the actual counterpart is dimmer,  $f \sim 2$ –4, unless the neutron star is at  $\lesssim 200 \text{ pc}$ .

## 5. Conclusions

We carefully re-analysed archival *VLT/FORS1* observations of the field of the XDINS RX J0420.0–5022, taken in 2000, and we performed deeper follow-up observations with *FORS2* in 2006 and in 2007. With a measured detection significance of  $\sim 2\sigma$  and a re-computed flux of  $B = 27.52 \pm 0.61$ , we can not rule out that the candidate counterpart tentatively detected in the *FORS1* images by Haberl et al. (2004) was a feature of the noisy sky background, produced by the very bright nearby star CD-50 1353. While we could not confirm this detection in our deeper *FORS2* images, we detected an apparently new feature ( $B = 27.5 \pm 0.3$ ) within the updated *Chandra* error circle of RX J0420.0–5022,  $\approx 0''.5$  north of the expected position of that detected in the *FORS1* images. Interestingly, both their similar flux and their angular separation, compatible with the upper limit on the RX J0420.0–5022 proper motion, suggest that we might have actually detected the same feature both in the *FORS1* and in the *FORS2* images. However, its still marginal detection significance ( $\sim 3.9\sigma$ ) makes it difficult to determine whether the latter feature is associated with a real object, and thus it is the RX J0420.0–5022 candidate counterpart, or it is also a possible background feature. From the flux of the putative counterpart we can rule out a  $> 7$  optical excess with respect to the extrapolation of the *XMM-Newton* spectrum. An optical excess of  $\sim 7$  (or lower) could be compatible either with rotation-powered emission from the neutron star magnetosphere or with thermal emission from the neutron star surface for a distance  $\lesssim 200 \text{ pc}$ , i.e. much lower than the current best estimate of  $\sim 350 \text{ pc}$  (Posselt et al. 2007). More observations are required to confirm the detection of the putative candidate counterpart and to validate its identification with RX J0420.0–5022. Unfortunately, the presence of star CD-50 1353 severely hampers ground-based follow-up observations, even if performed under sub-arcsec seeing conditions and using a very careful masking. High spatial resolution observations with the refurbished *Hubble Space Telescope* (*HST*), possibly to be performed in the ultraviolet, are the only way to settle the identification issue.

*Acknowledgements.* RPM acknowledges STFC for support through a Rolling Grant and thanks S. Moheler (ESO) for reducing our observations through the ESO data reduction pipeline and C. Izzo (ESO) for technical details. SZ acknowledges STFC for support through an Advanced Fellowship. We thank the anonymous referee for his/her comments to the manuscript.

## References

- Bertin, E. & Arnouts, S., 1996, A. & A. Suppl., 117, 393
- Cropper, M., Haberl, F., Zane, S., Zavlin, V. E., 2004, MNRAS, 351, 1099
- Fitzpatrick, E.L., 1999, PASP, 111, 63
- Grevesse, N. & Anders, E., 1989, AIPC, 183, 1
- Haberl, F., Motch, C., Buckley, D. A. H., Zickgraf, F.-J., Pietsch, W., 1997, A&A, 326, 662
- Haberl, F., Pietsch, W., Motch, C., 1999, A&A, 351, L53
- Haberl, F., Zavlin, V.E., 2002, A&A, 391, 571
- Haberl, F., Schwope, A. D., Hambaryan, V., Hasinger, G., Motch, C., 2003, A&A, 403, L19
- Haberl, F., Zavlin, V. E., Trümper, J., Burwitz, V., 2004, A&A 419, 1077
- Haberl, F., Motch, C., Zavlin, V. E., et al., 2004, A&A, 424, 635
- Haberl, F., 2007, Ap&SS, 308, 181
- Hambaryan, V., Hasinger, G., Schwope, A.D., Schulz, N.S., 2002, A&A, 381, 98
- Ho, W.C.G., et al. 2007, MNRAS, 375, 821

- Kaplan, D.L., Kulkarni, S.R., van Kerkwijk, M.H., 2002, *ApJ*, 579, L29
- Kaplan, D.L., Kulkarni, S.R., van Kerkwijk, M.H., 2003, *ApJ*, 588, L33
- Kaplan, D.L., van Kerkwijk, M.H., 2005a, *ApJ*, 628, L45
- Kaplan, D.L., van Kerkwijk, M.H., 2005b, *ApJ*, 635, L65
- Kaplan, D. L., 2008, *Proc. of "40 Years of Pulsars: Millisecond Pulsars, Magnetars, and More"*, AIP, 983, 331
- Kondratiev, V. I., Burgay, M., Possenti, A., et al., 2008, *Proc. of "40 Years of Pulsars: Millisecond Pulsars, Magnetars, and More"*, AIP, 983, 348
- Kulkarni, S. R. & van Kerkwijk, M. H., 1998, *ApJ*, 507, L49
- Lasker, B., Lattanzi, M. G., McLean, B. J., Bucciarelli, B., Drimmel, R., et al., 2008, *AJ*, 136, 735
- Lattanzi, M. G., Capetti, A., Macchetto, F. D. 1997, *A&A*, 318, 997
- Lo Curto, G., Mignani, R. P., Perna, R., et al. 2007, *A&A* 473, 539
- Malofeev, V. M., Malov, O. I., Teplykh, D. A., 2007, *Ap&SS*, 308, 211
- McLaughlin, M.A., Lyne, A.G., Lorimer, D.R. et al., 2006, *Nature*, 439, 817
- Mereghetti, S., 2008, *A&A Rev.*, 15, 225
- Mignani, R., Bagnulo, S., de Luca, A., et al., 2007a, *AP&SS*, 308, 203
- Mignani, R.P., Falomo, R., Moretti, A., Treves, A., Turolla, R., et al., 2008, *A&A*, 488, 267
- Motch, C., Haberl, F., 1998, *A&A*, 333, L59
- Motch, C., Zavlin, V.e., Haberl, F., 2003, *A&A*, 408, 323
- Motch, C., Sekiguchi, K., Haberl, F., Zavlin, V. E., et al., 2005, *A&A*, 429, 257
- Motch, C., Pires, A. M., Haberl, F., Schwope, A., Zavlin, V.E., 2009, *A&A*, 497, 423
- Perna, R., Hernquist, L., Narayan, R., 2000, *ApJ*, 541, 344
- Pires, A. M., Motch, C., Turolla, R., Treves, A., Popov, S. B., 2009, *A&A*, 498, 233
- Pons, J.A., Walter, F.M., Lattimer, J.M., Prakash, M., Neuäuser, R., An, P. 2002, *ApJ*, 564, 981
- Popov, S. B., Turolla, R. & Possenti, A. 2006, *MNRAS*, 369, L23
- Posselt, B., Popov, S. B., Haberl, F., et al., 2007, *Ap&SS*, 308, 171
- Posselt, B., Neuhäuser, R., Haberl, F., 2009, *A&A*, 496, 533
- Predehl, P. & Schmitt, J.H.M.M. 1995, *A&A* 293, 889
- Schwope, A., Erben, T., Kohnert, J., 2009, *A&A*, 499, 267
- Tiengo, A., Mereghetti, S., 2007, *ApJ*, 657, L101
- Walter, F.M., & Matthews, L.D., 1997, *Nature*, 389, 358
- Walter, F.M., 2001, *ApJ*, 549, 433
- van Kerkwijk, M.H., Kulkarni, S.R., 2001, *A&A*, 378, 986
- van Kerkwijk, M. H., et al., 2004, 608, 432
- van Kerkwijk, M. H., Kaplan, D. L., 2007, *Ap&SS*, 308, 191
- van Kerkwijk, M. H. & Kaplan, D. L., 2008, *ApJ*, 673, L163
- Wilms, J., Allen, A., McCray, R., 2000, *ApJ*, 542, 914
- Zane, S., Turolla, R., Drake, J.J., et al, 2004, *AdSpR*, 33, pp. 531-536.
- Zane, S., Cropper, M., Turolla, R., et al., 2005, *ApJ*, 627, 397
- Zane, S., De Luca, A., Mignani, R.P., Turolla, R., 2006, *A&A*, 457, 619
- Zane, S., Mignani, R.P., Turolla, R., et al., 2008, *ApJ*, 682, 487
- Zharikov, S., Shibanov, Yu., Komarova, V., 2006, *AdSpR*, 37, 1979